

# In-flight calibration of the Hinode EIS. Preliminary results. (Research Note)

G. Del Zanna

DAMTP, Centre for Mathematical Sciences, Wilberforce road Cambridge

Received ; accepted

## ABSTRACT

A preliminary assessment of the in-flight radiometric calibration of the Hinode EUV Imaging Spectrometer (EIS) is presented. This is done with the line ratio technique applied to a wide range of observations of the quiet Sun, active regions and flares from 2006 until 2012. Radiances over the quiet Sun are also considered. The responsivity of the EIS short-wavelength (SW) channel does not show significant degradation, with the exception of its shorter wavelengths. The responsivity of the EIS long-wavelength (LW) channel instead shows an overall degradation with time, with values at the start of the mission already lower by 30% than those measured on the ground. Some departures in the shapes of the ground calibration responsivities are also found. The net effect is that by the beginning of 2010 the responsivity of the LW channel was already a factor of two or more lower than the values measured on the ground. A first-order correction is proposed. With this correction, the main ratios of lines in the two channels become constant to within a relative 20%, and the He II 256 Å radiances over the quiet Sun also become constant over time. This correction removes long-standing discrepancies for a number of lines and ions, in particular those involving the strongest Fe X, Fe XIII, Fe XIV, Fe XVII and Fe XXIV lines, where discrepancies of factors of more than two were found. These results have important implications for various EIS science analyses, in particular for measurements of temperatures, emission measures and elemental abundances.

**Key words.** Atomic data – Line: identification – Sun: corona – Sun: abundances – Techniques: spectroscopic

## 1. Introduction

The Hinode EUV Imaging Spectrometer (EIS, see Culhane et al. 2007) with its two wavelength bands (SW: 166–212 Å; LW: 245–291 Å) observes emission lines from a wide range of ions, allowing detailed measurements since December 2006 of electron densities and temperatures, as well as emission measures and elemental abundances. For such measurements an accurate radiometric calibration is of paramount importance. EIS was radiometrically calibrated on the ground at RAL (UK) (Lang et al. 2006), providing an overall uncertainty of about 20%. It has been generally assumed that relative line intensities are measured by EIS with greater accuracy.

arXiv:1211.6771v1 [astro-ph.SR] 28 Nov 2012

A number of problems in the EIS intensities have been highlighted over the years, however, with typically factors of two discrepancies that could only be ascribed to calibration problems. Significant (50%) discrepancies were already found in 2007 August observations of the strong Fe XIII lines in the LW channel around 250 Å (Del Zanna 2011, 2012). They could not be ascribed to problems such as either blending or the atomic data, given that excellent agreement with e.g. the Malinovsky & Heroux (1973) [hereafter MH73] spectrum was found. Significant (50%) discrepancies were also found in a few of the strong Fe XIV lines (Del Zanna 2012). Again, they could only be ascribed to calibration problems.

Significant discrepancies in the Fe XVII 204.6 and 254.9 Å ratio were reported by Del Zanna (2008) and Del Zanna & Ishikawa (2009). These problems are not present in previous (Skylab) observations nor in laboratory measurements, where good agreement with theory is found (T. Watanabe, priv. comm.). The Fe XVII lines form a branching ratio, for which atomic data are very accurate.

Significant discrepancies in the two strongest flare diagnostic lines for EIS, the Fe XXIV 192.0 and 255.1 Å lines, were also reported by Del Zanna (2008). These discrepancies are present in the literature, although often not specifically mentioned. For example, Hara et al. (2011) presents a 2007 May 19 observation, where the doublet ratio is approximately 2.9 photons, instead of the expected (and well known) value of 1.85. Recent flare observations in 2012 (discussed below) have presented discrepancies of more than a factor of two for both Fe XVII and Fe XXIV ratios, suggesting that the discrepancy in the relative calibration between the SW and LW channels has increased over time. Problems in this important ratio have recently been confirmed by other authors (P. Young, H. Hara, priv. comm.).

Wang et al. (2011) performed a direct comparison between EIS SW and EUNIS quiet Sun [hereafter QS] observations in 2007, finding a small (20%) decrease compared to the ground calibration, a variation within the combined EUNIS and EIS uncertainties. An estimate of the relative responsivity at a few wavelengths in the LW channel was also performed, finding again overall consistency, but with larger uncertainties.

Starting in December 2006, regular observations of quiet Sun regions near Sun center have been taken to monitor EIS sensitivity changes. The initial studies (SYNOP001 and SYNOP002) downloaded the full EIS spectral range. However, after the X-band transmitter failure early in 2008, these were replaced with studies that only telemetered selected emission lines. The radiances of the He II 256 Å line show a clear decrease over time, and a preliminary long-term correction for all the EIS wavelengths was proposed, assuming that the He II radiances should stay constant over time (Mariska, priv. comm.). This was implemented in the EIS software. The sensitivity decay was modeled as an exponential decay of the form  $e^{-t/\tau}$  where  $t$  is the time of the observation in days since the Hinode launch (2006 September 22 21:36 UT), and  $\tau$  is the decay time, 1894 days (see EIS Software Notes #1,2).

Kamio & Mariska (2012) have recently presented QS radiances in EIS lines obtained from these synoptic studies. The EIS radiances were corrected for the sensitivity decay using an improved curve, still based on the He II radiances:  $(e^{-t/\tau_1} + e^{-t/\tau_2})/2$ , where the e-folding times  $\tau_1$  and  $\tau_2$  are 467 and 11311 days respectively. This correction was applied to both SW and LW channels, since no evidence for a variations between the SW and LW channels was found. The EIS radiances in lines formed above 1 MK show clear solar cycle trends, and the He II radiances become constant,

after the correction. However, low-temperature lines such as Fe VIII 185.2 Å and Si VII 275.3 Å show unrealistic increases (see Del Zanna et al. 2010a; Del Zanna & Andretta 2011 for a discussion on solar cycle effects on spectral lines), a clear indication of a problem in the correction.

The He II 256 Å is the strongest LW line in QS observations, and should stay relatively constant, although as shown in Del Zanna et al. (2010a); Del Zanna & Andretta (2011), the radiances of the helium lines are affected along the solar cycle by the coronal radiation, possibly because of photoionization-recombination effects (see references in Andretta et al. 2003). Large variations between quiet Sun and coronal hole areas are also present in helium lines. So, the use of the He II 256 Å for calibration is not ideal (see also below for further complications due to blending). It should be accurate, however, if proper QS observations are selected and the line carefully de-blended.

Mariska (2012) re-analysed the set of synoptic observations, noting that the radiances in the Fe VIII 185.2 Å, Si VII 275.3 Å, and Fe X 184.5 Å lines decreased in a similar way. The average decrease is small, of the order of 25%, corresponding to an e-folding time of  $7358 \pm 1030$  days. The He II 256 Å has a completely different behaviour, a nearly linear drop of a factor of 2 in the first two years of the mission, followed by a slower decay. The He II is severely blended, but these blends cannot explain the difference. Mariska (2012) suggested that the He II should be discarded, and that the results of the three above-mentioned lines indicate a slow decrease of *both* SW and LW channels over time.

A more complete analysis of the in-flight changes of the EIS responsivities is in principle possible using line ratios and not just line radiances, and the full EIS spectral range. The aim of this paper is to present preliminary results from such an analysis. Similar procedures adopted for the in-flight calibration of the SOHO CDS NIS and GIS channels (Del Zanna et al. 2001, 2010a) are followed here. Del Zanna et al. (2001) used the line ratio technique, described in more detail below, while Del Zanna et al. (2010a) showed that the radiances of low transition-region lines are relatively unchanged along the solar cycle and can be used to correct for the long-term degradation (these corrections have been adopted by the CDS team to produce the final calibrated NIS data for the whole SOHO mission).

The present analysis has only been possible now that we have a more complete understanding of the line identifications and the atomic data. Over the past ten years we<sup>1</sup> have calculated the atomic data for the main EIS lines and have provided them to the community via the CHIANTI database<sup>2</sup> (Dere et al. 1997; Landi et al. 2012). A review of line identifications and atomic data for all the EIS low-temperature lines was presented in Del Zanna (2009a). A review of line identifications and atomic data for all the EIS coronal lines was presented in Del Zanna (2012). The main flare lines were discussed in Del Zanna (2008), Del Zanna et al. (2011a), and Del Zanna & Ishikawa (2009). Several dozens of new lines have been identified, while similar numbers still await identification. The majority of the EIS spectral lines, despite the high spectral resolution, turned out to be blended, and for this calibration work a careful selection of the lines and observations needed to be done.

---

<sup>1</sup> UK APAP network [www.apap-network.org](http://www.apap-network.org)

<sup>2</sup> [www.chiantidatabase.org](http://www.chiantidatabase.org)

## 2. The method and the data

The method consists of choosing the appropriate observations and line ratios to constrain the relative responsivities of the instrument (Del Zanna et al. 2001). The method has been applied in many instances, not only for the SOHO CDS. For example, Neupert & Kastner (1983) used this method for an in-flight calibration of the OSO V and OSO VII EUV spectrometers. Brosius et al. (1998) also used the same method to calibrate observations from the Solar EUV Rocket Telescope and Spectrometer in 1995 (SERTS-95). Line ratios were also used by Young et al. (1998) to indicate problems in the calibration of the SERTS-89 active region spectrum (Thomas & Neupert 1994).

There are several good line ratios that can be used to check the in-flight relative calibration, as detailed below. The best are branching ratios, with typical uncertainties of 10% or less. But there are also a number of ratios useful for the calibration, those that have small variations with density and temperature. Each ratio was assessed against various atomic calculations and observations. The best calibrated EUV spectrum is that of MH73, which shows typical agreement with theory within a remarkable few percent.

The SW and LW channels have a sufficient number of line ratios to check the shape of their effective areas. The major difficulty and problem has been assessing the relative calibration between the two channels because very few line ratios are available. Another significant problem affect the use of data prior to 2008 Aug 24 (when the grating focus was adjusted). Until this date, there was an offset of about 2'' in the pointing of the SW and LW channels, meaning that the observations in the two channels were not simultaneous. Since most observations have been made with the 1'' slit, it took more than twice the exposure time to observe the same region. Most synoptic observations are single-slit observations, and there is no way to correct for this. Whenever raster observations have been available, co-spatial regions have been selected for the present work. The lack of co-spatiality limits the use of data prior to August 2008, in particular for the flare Fe xvii and Fe xxiv lines, since temporal variability is often significant on the exposure time scales.

A summary of the main line ratios chosen for the calibration is given in Table 1.

### 2.1. Fe viii and Fe ix

We use the atomic data and identifications of Fe viii given in Del Zanna (2009b) [a recent large-scale atomic calculation for this ion was performed by Tayal & Zatsarinny (2011), and a comparison with the Del Zanna (2009b) data has shown excellent agreement]. The Fe viii lines are only slightly dependent on the temperature, are strong and relatively free of blends in QS on-disk spectra (in active regions they are severely blended).

A few Fe ix from the  $3s^2 3p^4 3d^2$  configuration, identified by Young (2009), could be used for the calibration. There is relatively good agreement with theory (Storey et al. 2002) for these lines (Del Zanna 2009a), however they are not used for the present calibration, because work on other iron ions has shown the need for a larger calculation (which is in progress) for this ion.

### 2.2. Fe x

The Fe x identifications are summarised in Del Zanna et al. (2004). The recent atomic calculations of Del Zanna et al. (2012b) are adopted here. The new data significantly affect the 257.26 Å self-

**Table 1.** Line ratios used for the EIS calibration.

Line ratio (Å)	Theo (log Ne=8–9)	MH73	Det
Fe VIII 185.2 / 194.7	4.4		SW
Fe VIII 186.6 / 194.7	3.05		SW
Fe X 174.5 / 184.5	4.52–4.32	4.53	SW
Fe X 177.2 / 184.5	2.6–2.49	2.53	SW
Fe X 257.3 (sbl) / 184.5	1.52–1.12		SW/LW
Fe XI 178.1 / 182.2	0.27		BR SW
Fe XI 188.2 / 192.8	4.8		BR SW
Fe XI 202.7 / 188.3	0.144		BR SW
Fe XI 180.4 / 188.2	2.02		SW
Fe XI 257.5 (sbl) / 188.2	0.165		SW/LW
Fe XII 192.4 / 195.1 (sbl)	0.315		SW
Fe XII 193.5 / 195.1 (sbl)	0.67		SW
Fe XII 186.9 (sbl) / 196.6	3.49		SW
Fe XII 291/186.2	10.64–10.34		SW/LW
Fe XIII 209.6 / 200.	0.74–0.685		SW
Fe XIII 246.2 / 251.9	0.51	0.59	BR LW
Fe XIII 209.9 / 202.0	0.154		BR SW
Fe XIII 204.9 / 201.1	0.31	0.27	SW
Fe XIII 200.0 / 196.5	3.17–3.28	3.3	SW
Fe XIII 251.9 / 201.1	1.31		SW/LW
Fe XIV 252.2 / 264.8	0.23	0.25	BR LW
Fe XIV 289.1 / 274.2	0.064	0.063	BR LW
Fe XIV 274.2 / 211.3	0.69	0.77	SW/LW
Fe XIV 257.4 / 270.5	0.68		BR LW
Fe XIV 270.5 / (264.7+274.2)	0.26	0.26	LW
Fe XVI 251 / 263	0.57	0.66	LW
Fe XVI 263 / 265	10.2		LW
Fe XVII 204.7 / 254.9	0.93		BR SW/LW
Fe XXIV 192 / 255.1	1.85		SW/LW
Si VII 275.7 / 272.6	0.58		BR LW
Si X 253.8 / 258.4	0.19	0.18	BR LW
Si X 277.2 / 272.	0.84	0.87	BR LW
Si X 261.1 / 277.3	1.37–1.35	1.36	LW
S XI 285.6 (sbl) / 281.4	0.496		BR LW

**Notes.** The second column shows the theoretical ratios (photon units) within log Ne [cm<sup>-3</sup>]=8–9. The third column indicates the observed ratios from Malinovsky & Heroux (1973) [MH73]. The last column indicates if the ratio is a branching ratio (BR), and the EIS channel.

blend, the strongest Fe X line in the LW channel (identified in Del Zanna et al. 2004). One problem is that the ratio of this self-blend with the lines in the SW band is both slightly density and temperature sensitive, and is not ideal to check the SW/LW relative calibration. The 174.5, 177.2, 184.5 Å lines are all well observed in the SW channel. Their ratios do not depend on density or temperature, and excellent agreement (to within 10%) with the MH73 observations is found. QS observations, possibly off-limb, have been selected for these lines.

### 2.3. Fe XI

Fe XI produces a number of strong EIS lines. New identifications of many of them was presented in Del Zanna (2010), using the atomic calculations of Del Zanna et al. (2010b). A few temperature-sensitive lines around 255 Å were identified, in particular the self-blend at 257.5 Å. Excellent agreement with the MH73 data was found for a few Fe XI lines (Del Zanna 2010), providing confidence in the calculations, which resolved large (factors of 2-3) discrepancies. Here, the recent

large-scale atomic calculations of Del Zanna & Storey (2012a) are adopted. They have improved the atomic data for the lines around 255 Å.

The Fe XI 257.5 / 188.2 is a good cross-channel ratio, although it is slightly temperature-dependent. It varies by 14% in the  $\log T[K] = 6.0\text{--}6.1$  range. There are three good branching ratios in the SW channel. One of them, the 188.2 / 192.8 Å, is a complex one as discussed at length in Del Zanna (2010). The 188.2 is mainly due to Fe XI, while the 192.8 Å is blended with a host of O V lines (benchmarked in Del Zanna 2009a), and in active regions with Ca XVII. Off-limb QS observations have been used for this ratio, to avoid any blending. As discussed in Del Zanna (2010), there is a significant and puzzling disagreement in this Fe XI branching ratio (when the ground calibration is used).

#### 2.4. Fe XII

Several new identifications of important EIS Fe XII lines were presented in Del Zanna & Mason (2005), in particular the self-blends at 186.9 and 195.1 Å, used extensively to measure densities. Here, we use the large-scale atomic calculations of Del Zanna et al. (2012a), where we obtained significant improvements for the 186.9 and 196.5 Å lines over our previous calculations (Storey et al. 2005). The 192.4, 193.5, 195.1 Å are extremely strong in any observation and their ratios are not sensitive to density and temperature (at high densities the 195.1 Å does change), so they are excellent for the calibration. A large piece of dust on the EIS CCD affects the 193.5 Å line.

The 186.9 / 196.6 Å and the 291/186.2 Å ratios are only slightly dependent on density and are used here. The 291 and 186.2 Å lines are extremely weak and basically unobservable in most QS observations. Even their measurement in active regions had to be done carefully one spectrum at a time.

There are many other Fe XII lines, but they are either weak, strongly density-sensitive, or blended. For example, it has been suggested (P.Young, priv. comm.) that the 249.3 Å could be useful, however this line, identified in Del Zanna & Mason (2005), was found to be significantly blended.

#### 2.5. Fe XIII

There are several Fe XIII lines useful for the calibration. The new identifications presented in Del Zanna (2011) are adopted here, together with the atomic calculations of Storey & Zeippen (2010); Del Zanna & Storey (2012b). The Fe XIII lines are strong in off-limb QS and AR spectra, so only these observations have been considered. The 246.2 and 251.95 Å lines form a branching ratio, predicted at 0.51 (photons), in excellent agreement with MH73 (0.59). The 246.2 Å line is partly blended in on-disk observations. The observed intensities of the 246.2 and 251.95 Å were found too low by a factor of at least 1.5 (Del Zanna 2012), while they are in excellent agreement when the MH73 spectrum is considered. The 209.9 / 202.0 Å is also a good branching ratio. The 200.0 / 196.5 Å is a ratio that is not much dependent on density, so it is also used. Note that the 196.5 Å line is blended, mostly in on-disk observations. The 251.95 / 201 Å ratio varies only slightly with density and offers in principle a way to cross-calibrate the SW and LW channels. However, as pointed out in Del Zanna (2011), the atomic calculations for the 197.4, 201, and 204.9 Å lines, all originating from the same upper level, are uncertain, and some (small) discrepancies are present

even when the MH73 data are considered. The 197.4 Å line is blended and weak, and extreme care is needed to measure it.

## 2.6. Fe xiv

Fe xiv lines are of particular importance for the calibration of the LW channel and the cross-calibration between the SW and LW. Here we use the atomic data of Storey et al. (2000), but also consider Liang et al. (2010). Significant discrepancies due to calibration problems were found (Del Zanna 2012). Only AR observations are used here. In the QS, most of the Fe xiv lines are hardly visible and become severely blended. For example, a new Fe xi transition was identified by Del Zanna (2010) as blending the 264.7 Å line.

The 252.2 / 264.8 Å and 289.1 / 274.2 Å are good branching ratios, showing excellent agreement with the MH73 spectrum. The Fe xiv 257.4 / 270.5 Å branching ratio is predicted to be 0.68, but is often larger, a possible indication of a blend in the weaker 257.4 Å line. The ratio of the 270.5 / (264.7+274.2) lines is predicted to be 0.26 (phot), exactly as observed by MH73. The 274.2 / 211.3 Å ratio does not depend much on density and temperature. Good (within a relative 10%) agreement is found with the MH73 data. Note that the 274.2 Å is blended with a Si vii transition that has a strong density sensitivity. The intensity of this line has been roughly estimated as 0.2 the intensity of the 275.3 Å line.

## 2.7. Fe xvi, Fe xvii, and Fe xxiv

Fe xvi produces in active regions two strong lines, which are not density-sensitive and offer an excellent calibration ratio. We use the APAP atomic data of Liang et al. (2009b).

Fe xvii lines in the EIS channels have been identified/benchmarked in Del Zanna & Ishikawa (2009). Here, the atomic data of Liang & Badnell (2010) are used. The two main lines for this ions, at 204.7 and 254.9 Å, form a branching ratio. As the Fe xxiv 192 / 255.1 Å ratio, significant discrepancies were found by Del Zanna (2008) and Del Zanna & Ishikawa (2009), with the LW lines being much weaker than expected.

The Fe xvii 204.7 Å line was found by Del Zanna & Ishikawa (2009) to be blended with a low-temperature line, identified as partly due to Fe viii (Del Zanna 2009b). However, the blending did not resolve the issue. Opacity effects would make the problem worse, so the only explanation is a problem in the EIS calibration.

Flare observations of the right type are needed, to use Fe xvii and Fe xxiv lines for the calibration. Fe xvii and Fe xxiv are blended in small flares, as discussed in Del Zanna et al. 2011a. In large flares (M-class), the 192.0 Å line is normally saturated in the EIS observations. The Fe xxiv lines are strong during the impulsive phase of flares, but often exhibit strong blue-shifted components which complicate the analysis.

## 2.8. Silicon and sulfur lines

Si x lines are of particular importance for the calibration of the LW channel since they are among the strongest lines in quiet conditions, and there are three good ratios to use. We use the APAP atomic data of Liang et al. (2009a).

The Si VII 275.7 / 272.6 Å is a good branching ratio. There are no Si VII lines in the SW channel, however the temperature of formation of Si VII is close (slightly higher) than that of Fe VIII, and the ratio of lines from these ions are expected to be relatively constant.

The S X 257.1 / 264.2 ratio should in principle be a good ratio (0.348 photons), but the weak 257.1 Å line appears often blended. The S XI 285.6 / 281.4 Å is a good branching ratio in active region spectra.

## 2.9. Data selection and processing

The above discussion has made clear that a variety of targets were needed for the calibration. There are surprisingly few good observations suitable for such calibration purposes. Very few EIS studies telemetered the full spectral range. Most observations in the first few years were done with the 1" slit and very low counts in the QS are present. Upon my suggestion, spectral atlases with the 2" slit (and long exposures) have been run since 2010 for monitoring purposes (Atlas\_30, Atlas\_60, Atlas\_120). They have been extremely useful for the present work and should be continued.

A selection of QS data was chosen, by inspecting the spectra and avoiding observations with strong hot lines. This was relatively simple in the first three years of the mission, but since then very few QS observations have been made. One further complication is that the typical QS disappears at temperatures above 1 MK (Del Zanna & Andretta 2011) when solar activity increases. A variety of EIS studies were selected.

A selection of active region (AR) observations was also chosen, to use the ratios involving the Fe XII–Fe XVI ions (avoiding saturated areas). A full list is given in the Appendix.

To increase the signal-to-noise, observations with long exposures have been selected. These have the drawback of increasing the incidence of cosmic rays. The data had to be processed with custom-written software by visually inspecting each of the many thousands of exposures processed for cosmic ray hits. This was also necessary to avoid data dropouts or regions with high particle fluxes, a common feature in EIS observations. The number of 'hot' and 'warm' pixels in the EIS CCD has increased to a level such that since 2009 all observations need special processing. A complex interpolation procedure has been applied to all the data, before spatial averaging and line fitting.

Various geometrical corrections have been applied to the data (see Del Zanna 2009b for details). A 'slant' in the spectra was found in Del Zanna & Ishikawa (2009). This results in a wavelength dependent offset along the slit and has been corrected for by rotating each exposure and aligning the SW and LW channels.

Significant spatial averaging was needed, given the low signal in most exposures. Single-slit exposures were averaged along selected regions along the slit (typically over more than 100"), while raster observations were first analysed to select the best regions to obtain averaged spectra. The offset of about 2" in the pointing of the SW and LW channels prior to 2008 Aug 24 was also taken into account.

Each of the resulting spectra was wavelength calibrated (the EIS wavelength scale varies along the orbit). All the EIS lines were fitted with Gaussian profiles using the *cfit* package (Haugan 1997), directly on the raw spectra in data numbers (DN). One distinct feature of the EIS spectra is a variable 'bias'. In particular, the SW channel shows an enhanced 'background' in the center,



believed to be mostly due to a pseudo-continuum of spectral lines. The way the background is chosen affects the spectral fitting of the weak lines. Typical uncertainties in the lines are small, of the order of a few percent for the strong lines. Uncertainties were estimated by summing in quadrature the photon noise in the line and in the background. All the fits were checked visually.

For the conversion from data numbers (DN) to photon units, the EIS effective areas as available via *SolarSoft* were used (files *EIS\_EffArea\_A.004* and *EIS\_EffArea\_B.004*), and the gain of the CCD has been assumed equal to 6.3. These effective areas are the product of the aperture of the instrument ( $88.357 \text{ cm}^2$ ) by the efficiencies of the various optical components, which were all measured on the ground. During the ground calibration (Lang et al. 2006), significant discrepancies between the measured and predicted responsivities were found (for predicted we mean the values obtained by combining all the measured efficiencies of the various optical components). Scaling the predicted values (by a 1.6 factor) still left a discrepancy of about 20% between the SW and the LW channel, and about 50% within the LW channel. The end-to-end calibration only provided measurements at one wavelength for the SW ( $205.9 \text{ \AA}$ ) and four wavelengths for the LW ( $251.3, 256.3, 267.25, 283.4 \text{ \AA}$ ). The adopted EIS effective areas are based on these five calibration points, with account (for the SW) of the predicted shape of the responsivity.

### 3. Results

#### 3.1. SW and LW line radiances and ratios

We first present the averaged raw count rates in the QS areas in Fig. 1. The large scatter is mainly due to solar variability, however the cooler transition-region (hereafter TR) lines in the SW channel do show a remarkable constancy over time, indicative of no significant long-term degradation. The main line is the strong O v self-blend, close to the peak of the SW effective area, but other strong TR lines from S vi, Fe vii, Fe viii, Fe ix, all show the same trends. Having said that, lines short-ward of  $186 \text{ \AA}$  (such as O vi  $184.1 \text{ \AA}$ , shown in the figure) do show a decrease, indicative of a small decrease at the shorter wavelengths. This is further discussed below. The constancy of the TR line radiances and the direct EUNIS/EIS measurements of Wang et al. (2011) suggest that the *absolute SW central responsivity has not decreased significantly over time*. This is assumed in the remainder of the paper.

Note that this result is in stark contrast to the conclusions reached by Kamio & Mariska (2012) and Mariska (2012). It is interesting to note that excellent agreement (to within a relative 10%) between the EIS SW and the SDO AIA  $193 \text{ \AA}$  band was found in Del Zanna et al. (2011b). The AIA was independently calibrated on the ground, and the agreement indicates that the AIA  $193 \text{ \AA}$  band did not suffer significant degradation.

All the cool lines in the LW channel do however show a decrease in their QS radiances, as also shown in Fig. 1. The He ii  $256.3 \text{ \AA}$  line (which is actually a self-blend) is the strongest line in the channel and shows a marked decrease, by about a factor of two within the first two years.

The He ii  $256.3 \text{ \AA}$  line is severely blended with a host of transitions, mainly due to Si x, Fe x (Del Zanna et al. 2004), Fe xii (Del Zanna & Mason 2005), and Fe xiii (Del Zanna 2011). Careful deblending of off-limb observations indicates the possible presence of further minor blending. However, estimating the blends is not simple, as the lines are density-sensitive. Fortunately, the main contribution is from the Si x  $256.4 \text{ \AA}$  line, which forms a branching ratio with the Si x  $261 \text{ \AA}$

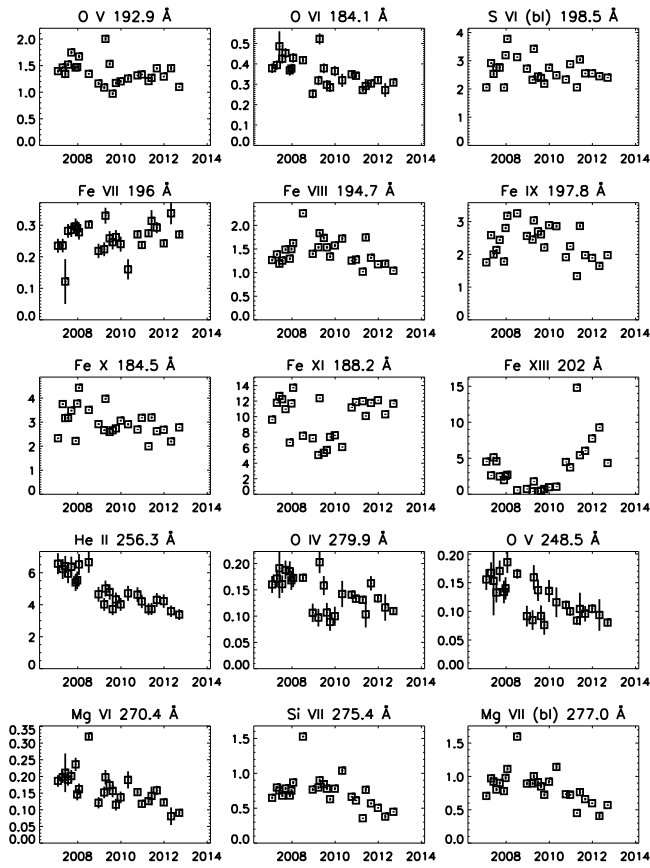


**Fig. 1.** Averaged EIS count rates (DN/s per 1'') in the QS areas as a function of time. The He II 256.3 Å line has been deblended.

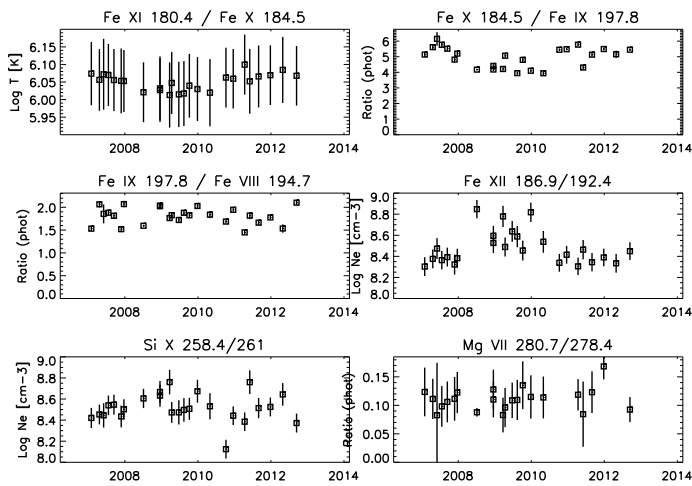


**Fig. 2.** Ratios of a few lines (photon units), with densities and temperatures obtained from them.

line, which can be estimated quite accurately. The broad profile of the He II blend was fitted with two Gaussians, leaving all parameters to vary. The total intensity in the blend was then obtained by summing the two intensities. The contributions from the other ions was then subtracted, using the measured (calibrated) intensities in the Si x 261, Fe x 257.2, Fe XII 192.4, and Fe XIII 252.0 Å lines. The result is that, in on-disk QS observations, the He II dominates by contributing over 80% to the

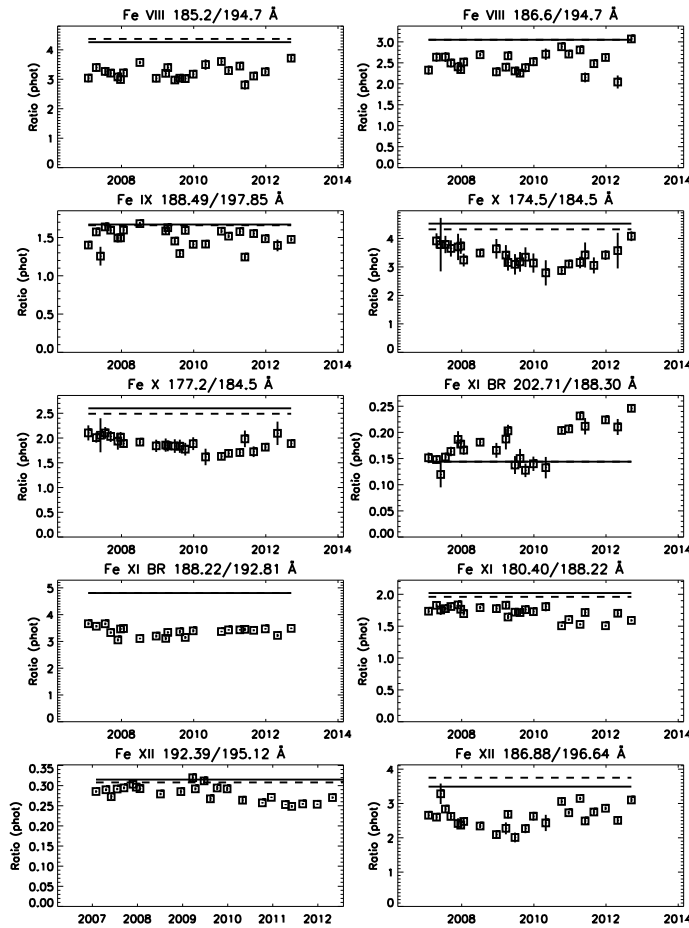


**Fig. 3.** Ratios of a few SW QS line radiances (photon units) using the ground calibration. Bars indicate the predicted values.

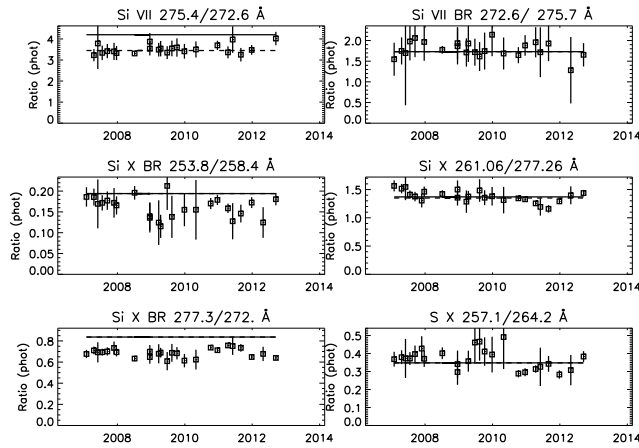


**Fig. 4.** Ratios of a few LW QS line radiances (photon units) using the ground calibration. Bars indicate the predicted values.

observed intensity. A similar result was found by Mariska (2012), where however the He II 256.3 Å line intensity was simply estimated by a double gaussian fit.

As pointed out by Kamio & Mariska (2012) and Mariska (2012), significant solar cycle changes are present in lines formed above 1 MK, (such as Fe XIII), as expected (Del Zanna et al. 2010a; Del Zanna & Andretta 2011). Before proceeding further, it is then important to estimate how the

solar cycle variations can affect densities and temperatures in the QS observations considered here. This is shown in Fig. 2. The count rates were converted into calibrated radiances (photon units) using the ground calibration. An estimate of the temperature was obtained from a Fe x 180.4 Å / Fe x 184.5 Å ratio, using CHIANTI v.6 ionization equilibrium. Very small changes within  $\log T[\text{K}]=6-6.1$  are present. Both lines most likely suffer degradation effects, but we assume that they are the same, since the lines are close in wavelength. Fe x / Fe ix and Fe ix / Fe viii ratios indicate very little changes in the TR temperature, as expected. Densities have also been measured from two among the best EIS ratios, one from Fe xii and one from Si x, using lines close in wavelength, to reduce degradation effects. The densities of the two ions agree very well (with the new atomic data), and show very little variability around  $\log n_e [\text{cm}^{-3}]=8.4$ . The Mg vii ratio (see Del Zanna 2009a for details on blending issues) also indicates no significant changes in the density of the QS transition region.

Figs. 3,4 show a selection of line ratios for the SW and LW channels, again using the ground calibration. Bars indicate the predicted values, for two different densities,  $\log n_e [\text{cm}^{-3}]=8$  (full lines) and  $\log n_e [\text{cm}^{-3}]=9$  (dashed lines).

The active region observations (both on-disk and off-limb cases have been considered) show similar results, offering more reliable branching ratios and better S/N. The ratios of a few AR line radiances are shown in Fig. 5. Overall, good agreement with the predicted ratios is found for the LW lines. Also, the ratios do not show significant trends. The situation is worse for the SW channel, where some puzzling variations are observed, and some significant departures from the expected values are present. The most affected region is towards the shorter wavelengths, where a small decrease over time in the line intensities is observed.

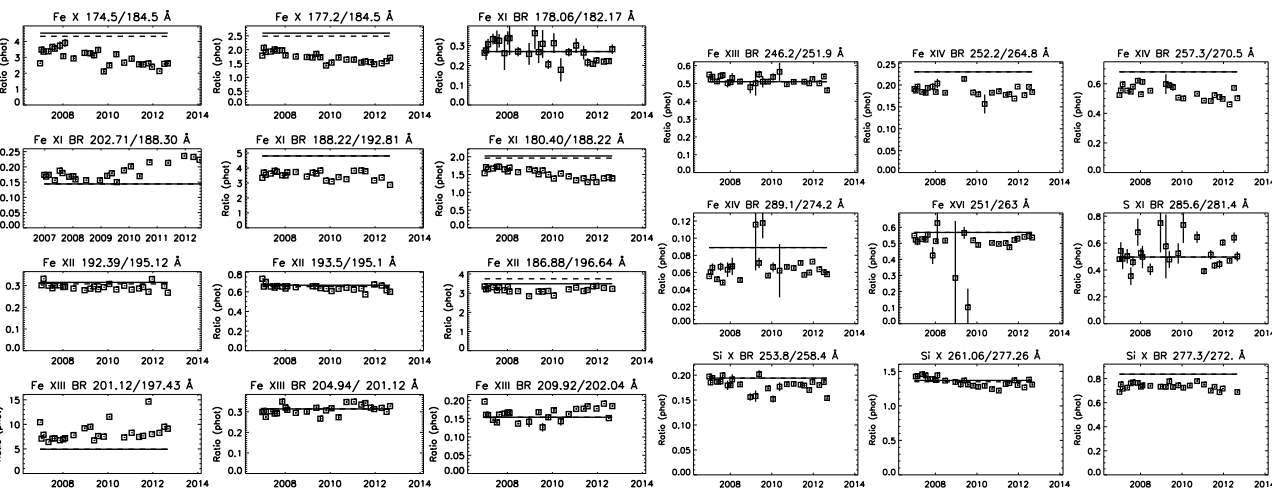


**Fig. 5.** Ratios of a few AR line radiances (photon units) in the SW and LW channels, obtained with the ground calibration. Bars indicate the predicted values.

### 3.2. SW/LW ratios and long-term correction

We now examine the cross-calibration between the SW and LW channels. All the ratios involving lines in the LW and SW channels show a decrease over time. Some of them also show (as already discussed in the introduction) a significant disagreement between observed and expected ratios even

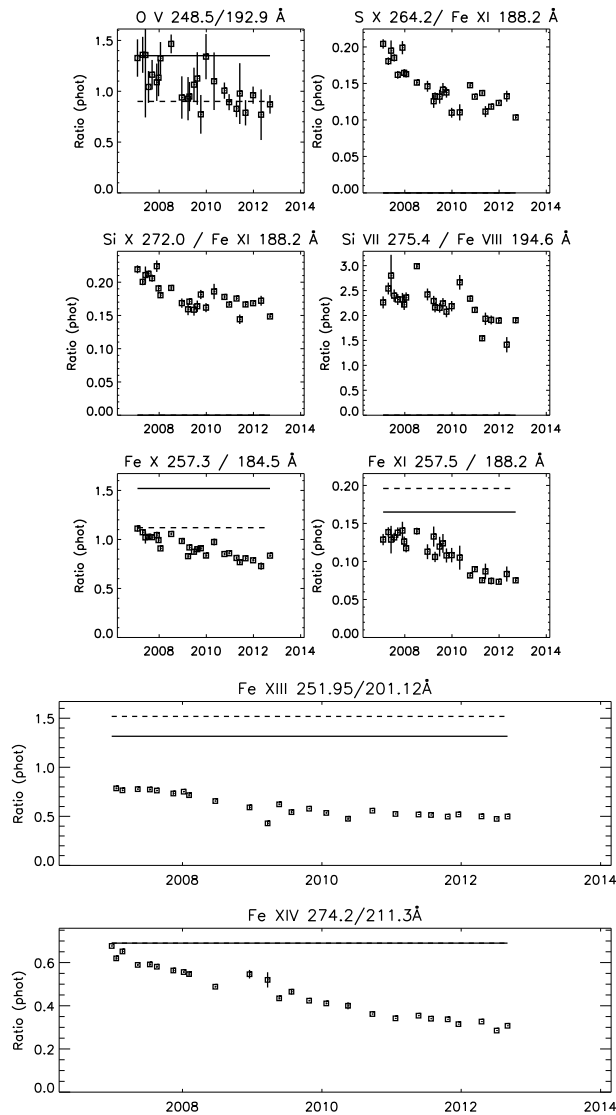


**Fig. 6.** Ratios of a few LW vs. SW line radiances (photon units) using the ground calibration. Bars indicate the predicted values. The top six plots shows the ratios from the QS observations, the lower ones are from the AR observations.

at the start of the mission. A selection of ratios, calculated using the ground calibration, is shown in Fig. 6. The O v ratio in Fig. 6 is not very reliable because the 248.5 Å is weak and because the ratios varies considerably with density. The S x 264.2 Å and the Si x 272 Å have an effective formation temperature for the quiet Sun that is close to Fe xi, hence are not expected to show large variations compared to Fe xi (even if they are different elements). Instead the ratios shown in Fig. 6 do show similar trends, i.e. a marked decrease in the first two years of the mission up to 2010.

The Si VII 275.4 Å/ Fe VIII 194.6 Å ratio is expected to be relatively constant because the density and temperature of the QS transition region does not seem to change much, and the relative abundance for silicon and iron is not expected to vary. However, the ratio has a slightly smaller decrease in time, compared to that one obtained from the Fe xi 257.5 / 188.2 Å ratio.

The Fe x ratio shown in Fig. 6 has some temperature and density dependence, however the expected variations based on the measured values are small (less than 10%), and cannot explain the differences with the Fe xi ratio. One explanation could be a decrease in the intensity of the 184.5 Å

line. This would be in line with the 40% decrease of the O VI 184.1 Å radiance, but not with the smaller (20%) decrease of the nearby 180.4 Å line (as indicated by the ratio with the 188.2 Å line).

Fig. 6 also shows that the ratios of Fe XIII and Fe XIV LW/SW lines are also decreasing over time as the previous ratios. These lines are very strong in AR spectra. The Fe XIV 274.2 / 211.3 Å decrease (a factor of more than two) is slightly steeper than that one measured from the Fe XI 257.5 / 188.2 Å ratio. The Fe XIV ratio is only slightly temperature sensitive, with an expected variation of much less than 10%. The 274.2 Å line is very close to the Si VII 275.4 Å one, which shows the opposite behaviour, a slower decrease with time. The Fe XIII 251.9 / 201.1 Å ratio instead shows a trend very similar to the Fe XI 257.5 / 188.2 Å one. Overall, the differences between the various ratios are at most within 20%, however.

To provide an estimate for the long-term drop in sensitivity, we have considered the Fe XI 257.5 / 188.2 Å ratio, which is mainly dependent only on temperature. We used the temperatures shown in Fig. 2 to estimate the expected ratio as a function of time (the density does not change significantly). The ratio between the observed and expected values is shown in Fig. 7. It shows a drop of almost a factor of two, but also a starting value in 2006 lower (by 30%) than the value based on the ground calibration, in agreement with the results mentioned in the introduction. The points were fitted with a linear plus a polynomial curve, which is assumed as our long-term correction for the LW channel.

The three other curves show for comparison the (normalised to the first point) exponential decays as available within the EIS software (dashed line), as suggested by Kamio & Mariska (2012) (dot-dashed line), and by Mariska (2012) (triple dot-dashed line).

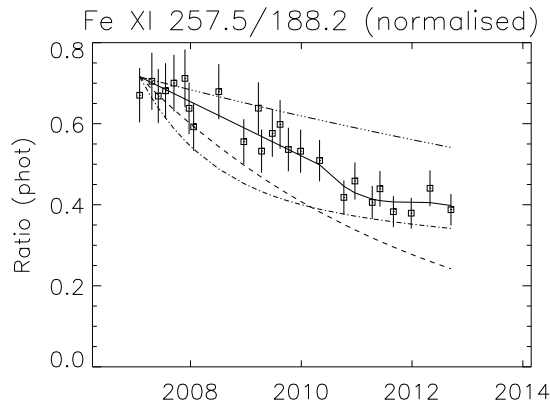


**Fig. 7.** Observed Fe XI 257.5 / 188.2 Å ratio, normalised by its expected variation over time, using the ground calibration (see text).

Fig. 8 shows that the long-term correction produces relatively constant radiances in the cool LW lines, most notably the He II 256.3 Å line (which has been deblended), but also the O IV, O V, and Mg VI. This confirms the reliability of the correction based on the line ratios. Some residual variations and a large scatter are present, but they could be due to solar variability.

Fig. 9 shows the ratios corrected for the long-term decrease in sensitivity. The correction based on the Fe XI 257.5 / 188.2 Å reproduces quite well (within 20%) the Fe XIII and Fe XIV ratios, the latter being the most reliable of all in terms of atomic data. The small increase in the Fe X 257.3/184.5 Å is partly to be ascribed to a decrease in the effective area at 184 Å not taken into

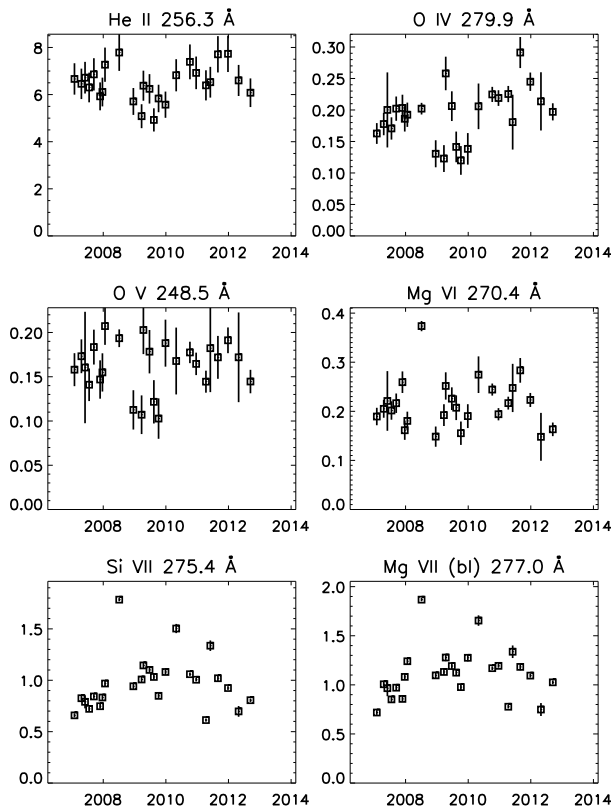


**Fig. 8.** Averaged EIS count rates (DN/s per  $1''$ ) in the QS areas, corrected for the LW long-term decrease in sensitivity.

account. The O v ratios shows an overall constancy, as well as the S x vs. Fe x1 and the Si x vs. Fe x1 until 2010. The increases after 2010 are probably related to solar cycle effects, when the temperature structure of the QS above 1 MK changes significantly. The Si VII 275.4 Å/ Fe VIII 194.6 Å corrected ratio shows a residual increase over time. Again some solar cycle effects cannot be excluded here, although are difficult to assess given that the formation temperature of Fe VIII is uncertain, having changed significantly over the years, due to new calculations and measurements of ionization and recombination rates.

### 3.3. An estimate of the in-flight effective areas

The various line ratios have unfortunately shown some clear departures from the ground calibration, so all the information from the various line ratios has been collected for a selection of dates to try and find a correction to the ground calibration. Clearly, given the overall drop in LW sensitivity, it would be important to assess the responsivities during the first month of routine observations. A QS observation on 2006 Dec 23 was selected, with two regions, one on-disk and one off-limb. An AR on-disk observation of hot core loops on 2006 Dec 25 was also selected, to build ratios of the hotter lines. The relative constancy (early on) of the various branching ratios means that the results can be extended to the first years of the mission.

For the flare lines, a suitable observation was searched but not found. The search criteria were to find any EIS flare observation within the first 8 months of at least a C-class flare and which

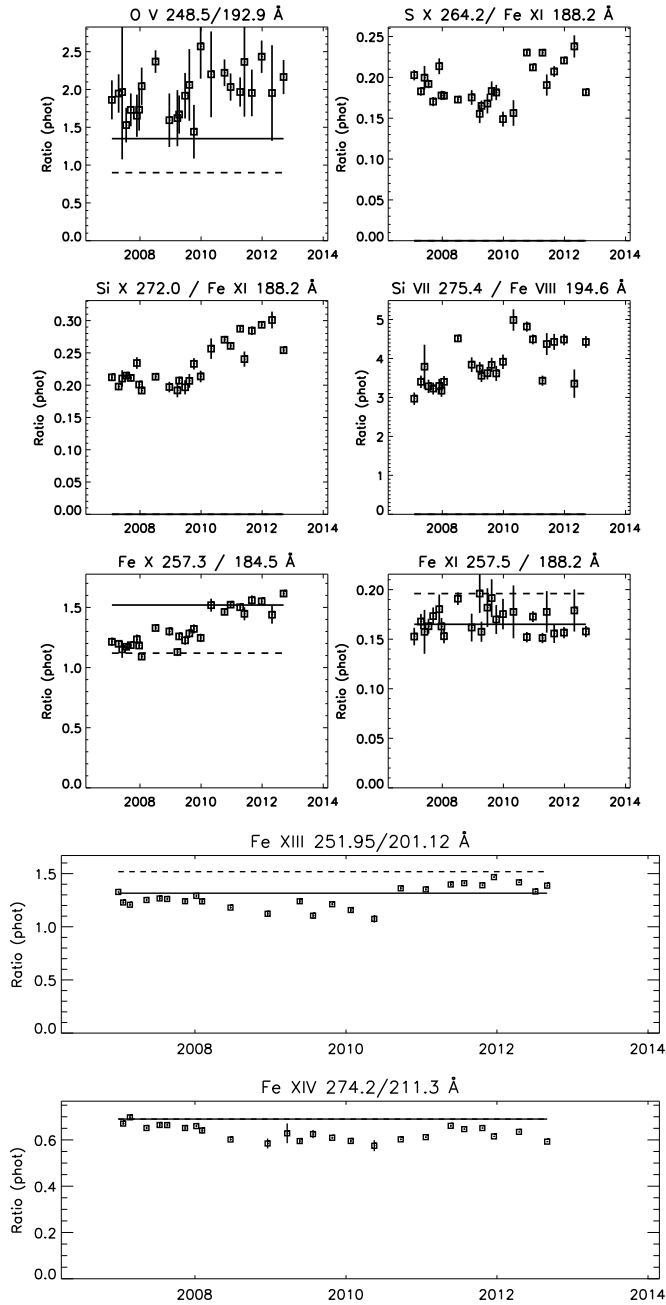


**Fig. 9.** Ratios of a few QS and AR line radiances (photon units) in the SW and LW channels, obtained with the ground calibration and corrected for the LW long-term decrease in sensitivity. Bars indicate the predicted values.

contained the two Fe xvii and Fe xxiv line ratios. So, the observations of 2007 Jun 2 discussed in Del Zanna (2008) are considered here.

Each observed and theoretical line ratio considered produces a constraint to the relative values of the effective areas. The values obtained from the 2006 Dec 23,25 and 2007 Jun 2 observations (DN/s in the lines) are shown in Fig. 10. One of the lines (triangle) is shown as a reference, with its value normalised to the effective area. The other line (square) of the ratio is linked to the previous one. We have assumed that the effective areas near 195 Å (the peak) are the same as those of



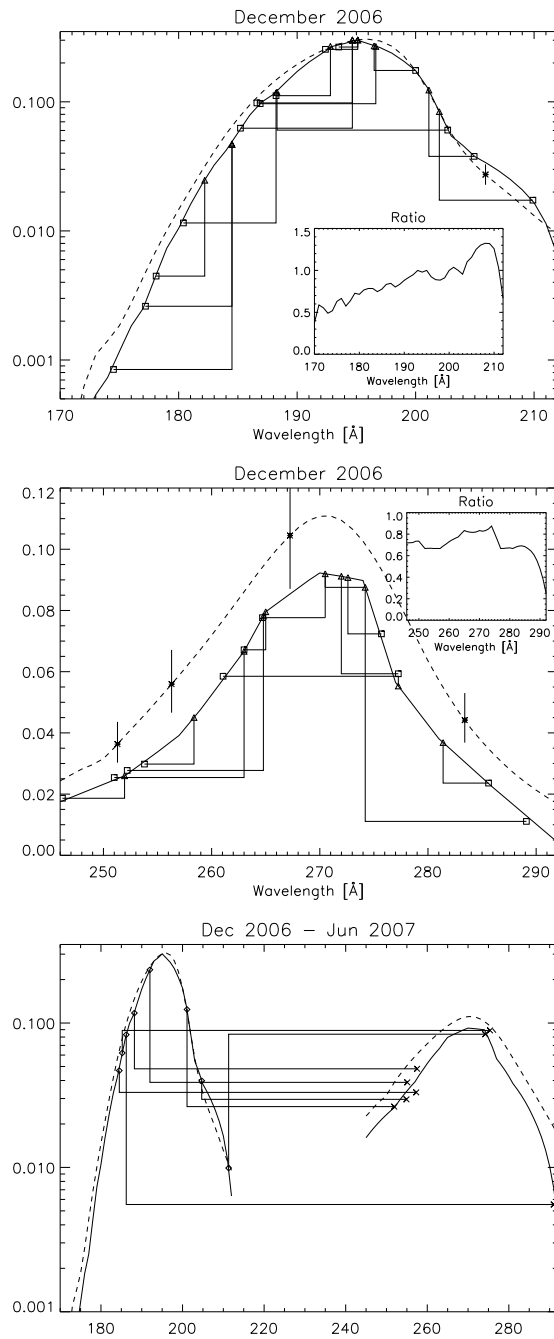


**Fig. 10.** Effective areas for the EIS channels obtained from the 2006 Dec 23,25 and 2007 Jun 2 observations. The full lines indicate the proposed values, while the dashed ones indicate those from the ground calibration. The two plots above show the line ratios used for the SW and LW channels separately, while the bottom plot shows the cross-channel line ratios. The asterisks show the five measurements of the ground calibration. The insets show the ratios between the measured and the ground calibration.

the ground calibration. The five ground calibration measurements are also shown, with their 20% uncertainty.

The results for the SW channel are shown in logarithmic scale. Good agreement with the ground calibration (dashed line) is found in the central region, although large departures of up to a factor

of two are found elsewhere. The longer wavelengths are constrained up to 210 Å (with a reliable Fe xiii branching ratio), and the drop at 211 Å is to bring the Fe xiv 211.3 Å into agreement with the Fe xiv LW lines. The shorter wavelengths are well constrained by various ratios, indicating a consistent departure from the ground calibration. The LW effective areas are in good agreement with those from the ground calibration, with the exception of wavelengths longer than 285 Å, and an overall drop of 20–30%.

A detailed emission measure analysis was performed on the off-limb quiet Sun observation of 2006 Dec 23. Excellent agreement between all the SW and LW lines was found, further confirming the new calibration. The results of this analysis are not presented here since they would require a lengthy discussion of all the blends and the lines.

A similar line ratio study was performed with the 2007 Aug 19 AR observations discussed in detail in Del Zanna (2012). Again the results are not presented here. Aside from a further drop of 10% in the LW effective area, large departures in the shapes of the SW and LW effective areas were not found. The new effective areas remove all the main discrepancies discussed in Del Zanna (2012).

As a *first-order calibration* we assume in the remainder that: a) the SW effective areas do not change over time; b) the shapes of the SW and LW effective areas are as shown in Fig. 10; c) the LW effective areas decrease over time as shown by the fit in Fig. 7.

Several recent observations in 2012 were then analysed, to see if this first order calibration is sufficient to remove the main problems. We present here only the results of the analysis of an off-limb AR observation of 2012 Apr 16 and a flare observation of 2012 Mar 9. The March and April 2012 observations have been combined in Fig. 11, using the proposed first-order calibration. The figure indicates that large departures in the shapes of the effective areas have not occurred, with the exception of the shorter wavelengths of the SW channel, consistently with the behaviour of the line ratios discussed previously. By this time, the long-wavelength edge of the LW channel has a responsivity five times lower compared to the ground calibration.

The 2012 Mar 9 observation is particularly important since it is the first and only EIS full-spectral observation of a medium-size M-class flare. A detailed description of this observation is presented in a separate paper. Here, we focus on the Fe xvii and Fe xxiv lines.

Extra care was needed to select the best spectra for either Fe xvii or Fe xxiv. For example, various lines were saturated in many exposures. The Fe xxiv lines during the impulsive phase have large blue-shifted components which complicate the analysis. A spectrum for Fe xvii and one for Fe xxiv was obtained. In the first spectrum, the Fe xvii lines are so bright that significant blending should not be present. The Fe xvii lines are very useful to check the calibration because they fall across most LW wavelengths. Discrepancies of over a factor of two were found in the Fe xvii 204.7 / 254.9 Å and Fe xxiv 192 / 255.1 Å ratios using the ground calibration. The first-order calibration presented above removes these main discrepancies.

Fig. 12 shows the emissivity ratio curves relative to the main Fe xvii lines. These emissivity ratio curves are obtained by dividing the observed intensity  $I_{\text{ob}}$  of a line by its emissivity:

$$F_{ji} = \frac{I_{\text{ob}} N_e C}{N_j(N_e, T_e) A_{ji}} \quad (1)$$

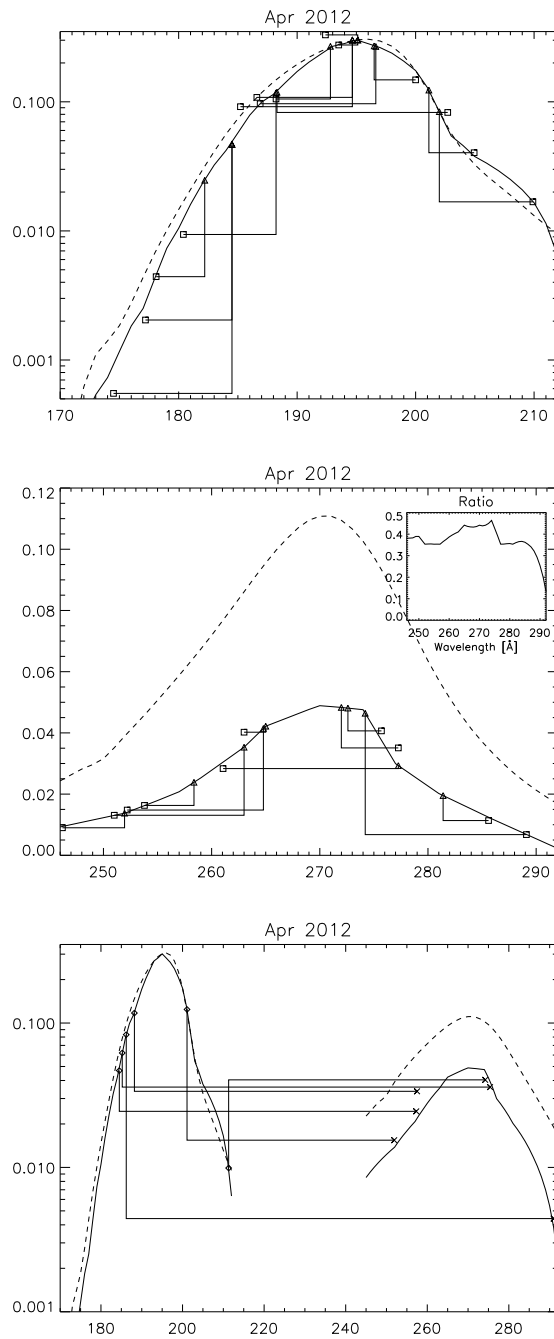


**Fig. 11.** Effective areas for the EIS channels obtained from the 2012 Apr 16 and Mar 9 observations. The full lines indicate the proposed values, while the dashed ones indicate those from the ground calibration. The two plots above show the line ratios used for the SW and LW channels separately, while the bottom plot shows the cross-channel line ratios.

calculated at a fixed electron density  $N_e$  and plotted as a function of the temperature  $T_e$  (see Del Zanna et al. 2004 for details). The scaling constant  $C$  is chosen so that the 254.9 Å curve is close to unity.

The emissivity ratio curves show the large discrepancy (more than a factor of two) in the Fe xvii 204.7 / 254.9 Å branching ratio, when the current ground calibration is adopted. The present first-order calibration brings the ratio within a very reasonable 20%, although the plot also shows that

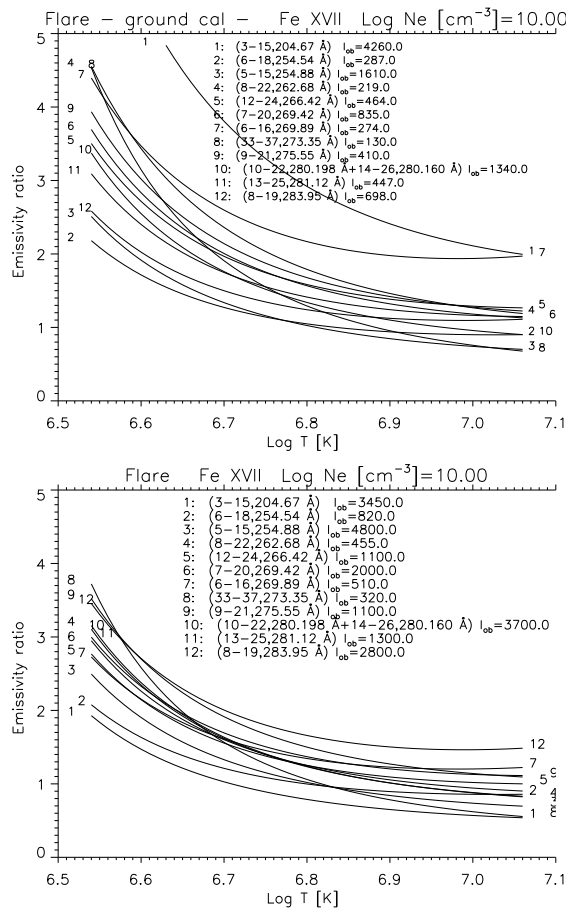


**Fig. 12.** Emissivity ratio curves relative to the main Fe XVII EUV transitions observed by Hinode EIS on 2012 Mar 9.  $I_{ob}$  is the calibrated observed intensity in photons  $\text{cm}^{-2} \text{s}^{-1} \text{arcsec}^{-2}$ . The top plot shows the results with the current ground calibration, while the bottom one with the present first-order correction.

further corrections might be necessary to bring all the radiances into agreement (although some might be due to the atomic data or blending – further work is in progress to clarify this issue). The plot also shows that the Fe XVII lines can potentially be used to measure electron temperatures for flares, once all the calibration problems are sorted out. This is a remarkable new diagnostic.

In the Fe XXIV spectrum, the Fe XXIV 192 / 255.1 Å ratio is about 4 (photon units) if the ground calibration is used, instead of the expected 1.85. The present first-order calibration brings the ratio down to a value of 1.5, i.e. within a reasonable 20% the expected value.

#### 4. Conclusions

This preliminary assessment of the in-flight degradation of the EIS instrument based on line radiances and ratios shows a consistent pattern that is fundamentally different from what has been assumed so far.

The observations show a clear degradation of the long-wavelength channel, compared to the short-wavelength one. The responsivity of the LW channel in December 2006 was already lower (by 20–30%) than what was measured on the ground, and continued to decrease significantly until

2010, when radiances in LW lines become underestimated by a factor of 2. On the other hand, QS radiances in SW lines do not show any indication of a major degradation for the SW channel.

Overall, the shapes of the effective areas in their central regions are consistent with those measured on the ground, especially considering the large differences (up to 50%) in the ground measurements. Significant departures are present towards the edges of both SW and LW channels, however. Further work will be needed to better assess the wavelength dependency of the degradation. This degradation appears to have leveled off after 2010, which is encouraging.

The present LW long-term correction based on the Fe XI 257.5 / 188.2 Å ratio brings the main LW/SW line ratios to become constant to within a reasonable 20%, and also produces relatively constant QS radiances in the LW cool lines, most notably the strongest line, He II 256.3 Å.

The present new calibration removes a number of peculiar features in terms of emission measures and elemental abundances that we have encountered. A significant number of studies such as those concerning emission measures combine the use of EIS cooler lines (e.g. Fe VIII – Fe XIII) from the SW channel with the hotter ones (Fe XIV–Fe XVI) from the LW channel. Such studies should be revised by taking into account the decrease in the responsivity of the LW channel.

Out-gassing and contamination of the entrance filter could be the cause of the observed degradation. Deposition of carbon compounds is common, and would cause an enhanced degradation in the LW channel, compared to the SW one.

Significant decreases in responsivities are typical for EUV/UV space instruments, especially those with entrance filters. Large degradations (order of magnitude) are very common, even in recent instruments (BenMoussa et al. 2012). For example, already at first light, the SDO EVE MEGS-B showed a factor of 10 drop in sensitivity, and large decreases are still occurring. The EIS instrument has performed reasonably well in this respect, with only a factor of two degradation in one of the channels within the first two years.

There is an on-going effort within the EIS team to understand the causes of this degradation and to provide the best possible correction to the EIS users. The present work is a contribution to this effort. The proposed calibration will be made available to the EIS users. In the near future, a new EUNIS calibration rocket should be launched, which will provide important information on the current EIS calibration.

*Acknowledgements.* Useful discussions and comments from various members of the EIS team are acknowledged, in particular from P. Young, J. Mariska, T. Watanabe, H. Hara., H. Warren

Support from STFC is acknowledged. The work of the UK APAP Network was funded by the UK STFC under grant No. PP/E001254/1 with the University of Strathclyde. CHIANTI is a collaborative project involving researchers at the Universities of Cambridge (UK), George Mason, Michigan (USA). The excellent Hinode Science Data Centre Europe was used to search the EIS database.

Hinode is a Japanese mission developed and launched by ISAS/JAXA, with NAOJ as domestic partner and NASA and STFC (UK) as international partners. It is operated by these agencies in co-operation with ESA and NSC (Norway).

## References

- Andretta, V., Del Zanna, G., & Jordan, S. D. 2003, *A&A*, 400, 737  
BenMoussa, A., Gissot, S., Schuhle, U., & Del Zanna, G. 2012, *Sol. Phys.*, submitted  
Brosius, J. W., Davila, J. M., & Thomas, R. J. 1998, *ApJ*, 497, L113+  
Culhane, J. L., Harra, L. K., James, A. M., et al. 2007, *Sol. Phys.*, 60

- Del Zanna, G. 2008, A&A, 481, L69  
Del Zanna, G. 2009a, A&A, 508, 501  
Del Zanna, G. 2009b, A&A, 508, 513  
Del Zanna, G. 2010, A&A, 514, A41+  
Del Zanna, G. 2011, A&A, 533  
Del Zanna, G. 2012, A&A, 537, A38  
Del Zanna, G. & Andretta, V. 2011, A&A, 528, A139+  
Del Zanna, G., Andretta, V., Chamberlin, P. C., Woods, T. N., & Thompson, W. T. 2010a, A&A, 518, A49+  
Del Zanna, G., Berrington, K. A., & Mason, H. E. 2004, A&A, 422, 731  
Del Zanna, G., Bromage, B. J. I., Landi, E., & Landini, M. 2001, A&A, 379, 708  
Del Zanna, G. & Ishikawa, Y. 2009, A&A, 508, 1517  
Del Zanna, G. & Mason, H. E. 2005, A&A, 433, 731  
Del Zanna, G., Mitra-Kraev, U., Bradshaw, S. J., Mason, H. E., & Asai, A. 2011a, A&A, 526, A1+  
Del Zanna, G., O'Dwyer, B., & Mason, H. E. 2011b, A&A, 535, A46  
Del Zanna, G. & Storey, P. J. 2012a, A&A, submitted  
Del Zanna, G. & Storey, P. J. 2012b, A&A, 543, A144  
Del Zanna, G., Storey, P. J., Badnell, N. R., & Mason, H. E. 2012a, A&A, 543, A139  
Del Zanna, G., Storey, P. J., Badnell, N. R., & Mason, H. E. 2012b, A&A, 541, A90  
Del Zanna, G., Storey, P. J., & Mason, H. E. 2010b, A&A, 514, A40+  
Dere, K. P., Landi, E., Mason, H. E., Monsignori Fossi, B. C., & Young, P. R. 1997, A&AS, 125, 149  
Hara, H., Watanabe, T., Harra, L. K., Culhane, J. L., & Young, P. R. 2011, ApJ, 741, 107  
Haugan, S. V. H. 1997, CDS software note, 47  
Kamio, S. & Mariska, J. T. 2012, Sol. Phys., 279, 419  
Landi, E., Del Zanna, G., Young, P. R., Dere, K. P., & Mason, H. E. 2012, ApJ, 744, 99  
Lang, J., Kent, B. J., Paustian, W., et al. 2006, Appl. Opt., 45, 8689  
Liang, G. Y. & Badnell, N. R. 2010, A&A, 518, A64+  
Liang, G. Y., Badnell, N. R., Crespo López-Urrutia, J. R., et al. 2010, ApJS, 190, 322  
Liang, G. Y., Whiteford, A. D., & Badnell, N. R. 2009a, A&A, 499, 943  
Liang, G. Y., Whiteford, A. D., & Badnell, N. R. 2009b, A&A, 500, 1263  
Malinovsky, L. & Heroux, M. 1973, ApJ, 181, 1009  
Mariska, J. 2012, Sol. Phys., submitted  
Neupert, W. M. & Kastner, S. O. 1983, A&A, 128, 181  
Storey, P. J., Del Zanna, G., Mason, H. E., & Zeippen, C. 2005, A&A, 433, 717  
Storey, P. J., Mason, H. E., & Young, P. R. 2000, A&AS, 141, 285  
Storey, P. J. & Zeippen, C. J. 2010, A&A, 511, A78+  
Storey, P. J., Zeippen, C. J., & Le Dourneuf, M. 2002, A&A, 394, 753  
Tayal, S. S. & Zatsarinny, O. 2011, ApJ, 743, 206  
Thomas, R. J. & Neupert, W. M. 1994, ApJS, 91, 461  
Wang, T., Thomas, R. J., Brosius, J. W., et al. 2011, ApJS, 197, 32  
Young, P. R. 2009, ApJ, 691, L77  
Young, P. R., Landi, E., & Thomas, R. J. 1998, A&A, 329, 291

## Appendix A: List of the observations

**Table A.1.** QS observations used for the EIS calibration.

File	Raster	Slit (")	Exp. (s)	FOV (")
20061223_161013	HPW001_FULLCCD_RAST	1	90	128×128
20061231_215548	SYNOPSIS01_slit	1	90	1×256
20070114_220819	SYNOPSIS01_slit	1	90	1×256
20070130_111912	HPW001_FULLCCD_RAST	1	90	128×128
20070216_112350	SYNOPSIS01_slit	1	90	1×256
20070316_180127	SYNOPSIS01_slit	1	90	1×256
20070421_000705	SYNOPSIS01_slit	1	90	1×256
20070421_030643	SYNOPSIS02_FULLCCD	1	90	128×184
20070517_000450	SYNOPSIS01_slit	1	90	1×256
20070602_131520	HPW008_FULLCCD_RAST	1	25	128×128
20070620_180835	SYNOPSIS01_slit	1	90	1×256
20070720_110822	SYNOPSIS01_slit	1	90	1×256
20070817_062935	SYNOPSIS01_slit	1	90	1×256
20070913_175836	SYNOPSIS01_slit	1	90	1×256
20071024_061835	SYNOPSIS01_slit	1	90	1×256
20071125_104656	SYNOPSIS01_slit	1	90	1×256
20071222_111205	SYNOPSIS01_slit	1	90	1×256
20080121_160213	SYNOPSIS02_FULLCCD	1	90	128×184
20080123_095235	SYNOPSIS01_slit	1	90	1×256
20080705_112034	FELDMAN_QSCH_ATLASv1	2	120	24×304
20081217_110519	HPW001_FULLCCD_RAST	1	90	128×128
20090323_174230	SYNOPSIS01_slit	1	90	1×256
20090413_175041	HPW001_FULLCCD_RAST	1	90	128×128
20090414_180730	SYNOPSIS01_slit	1	90	1×256
20090511_180929	SYNOPSIS01_slit	1	90	1×256
20090623_182812	SYNOPSIS01_slit	1	90	1×256
20090720_060035	SYNOPSIS01_slit	1	90	1×256
20090813_180429	SYNOPSIS01_slit	1	90	1×256
20090919_180557	SYNOPSIS01_slit	1	90	1×256
20091007_120219	HPW001_FULLCCD_RAST	1	90	128×128
20091023_060550	SYNOPSIS01_slit	1	90	1×256
20091113_180529	SYNOPSIS01_slit	1	90	1×256
20091227_063535	SYNOPSIS01_slit	1	90	1×256
20100501_054013	Atlas_30	2	30	120×160
20101008_101526	Atlas_120	2	120	120×160
20101220_050526	Atlas_120	2	120	120×160
20110413_132033	Atlas_120	2	120	120×160
20110603_113020	Atlas_060x512_60s	1	60	60×512
20110831_054534	Atlas_60	2	60	120×160
20111226_181940	Atlas_120	2	120	120×160
20120428_151319	Atlas_060x512_60s	1	60	60×512
20120913_182534	Atlas_120	2	120	120×160

**Notes.** The columns indicate the file name (date and UT time), the EIS raster acronym, the slit used, the exposure time and the field of view (FOV) of the observation.

**Table A.2.** AR observations used for the EIS calibration.

File	Raster	Slit (")	Exp. (s)	FOV (")
20061225_221058	SYNOP001_slit	1	90	1×256
20061225_225013	HPW001_FULLCCD_RAST	1	90	128×128
20070118_120435	SYNOP001_slit	1	90	1×256
20070210_000119	SYNOP001_slit	1	90	1×256
20070220_054028	SYNOP001_slit	1	90	1×256
20070322_125559	SYNOP001_slit	1	90	1×256
20070423_184443	SYNOP001_slit	1	90	1×256
20070511_105544	SYNOP001_slit	1	90	1×256
20070519_180450	SYNOP001_slit	1	90	1×256
20070607_181319	SYNOP001_slit	1	90	1×256
20070630_175020	SYNOP001_slit	1	90	1×256
20070630_175235	SYNOP001_slit	1	90	1×256
20070630_175451	SYNOP001_slit	1	90	1×256
20070630_175706	SYNOP001_slit	1	90	1×256
20070714_000949	SYNOP001_slit	1	90	1×256
20070819_133227	HPW001_FULLCCD_RAST	1	90	128×128
20070929_102529	SYNOP001_slit	1	90	1×256
20071020_021049	SYNOP001_slit	1	90	1×256
20071114_000707	SYNOP001_slit	1	90	1×256
20071206_175549	SYNOP001_slit	1	90	1×256
20080107_101448	SYNOP001_slit	1	90	1×256
20080118_103435	SYNOP001_slit	1	90	1×256
20080204_104700	SYNOP001_slit	1	90	1×256
20080620_230339	HPW001_FULLCCD_RAST	1	90	128×128
20081217_110519	HPW001_FULLCCD_RAST	1	90	128×128
20090322_060630	SYNOP001_slit	1	90	1×256
20090521_180529	SYNOP001_slit	1	90	1×256
20090725_055049	SYNOP001_slit	1	90	1×256
20091025_214625	HPW008_FULLCCD_RAST	1	25	128×128
20100123_171532	SYNOP001_slit	1	30	1×256
20100517_135741	Atlas_60	2	60	120×160
20100922_112633	Atlas_60	2	60	120×160
20110121_123757	Atlas_60	2	60	120×160
20110522_103354	Atlas_60	2	60	120×160
20110726_175935	Atlas_60	2	60	120×160
20111022_100543	Atlas_60	2	60	120×160
20111217_125856	Atlas_60	2	60	120×160
20120416_124033	Atlas_60	2	60	120×160
20120704_223657	Atlas_60	2	60	120×160
20120830_234044	Atlas_60	2	60	120×160